Generation Mechanism of Near-Fault Ground Motion Pulses for Dip-Slip Faulting

N. Poiata
Earthquake Research Insitute, University of Tokyo, Japan
Now at Institute de Physique du Globe de Paris, France

H. Miyake
Earthquake Research Insitute, University of Tokyo, Japan

K. Koketsu
Earthquake Research Insitute, University of Tokyo, Japan

SUMMARY:
We studied main aspects of the rupture configuration contributing to the generation of near-fault ground motion pulses during a dip-slip faulting event, by performing the forward simulations in broadband and low-frequency ranges for the different rupture scenarios of the 2009 L'Aquila, Italy (M_w 6.3) earthquake. The rupture scenarios are assumed on the bases of the broadband source model determined by Poiata *et al.* (2012). We could identify the rupture directivity effect, the radial rupture propagation towards the site, and the focusing effect (Kagawa, 2009) as being the main mechanisms contributing to the generation of the near-fault ground motion pulses. Predominance of one of these mechanisms was estimated to depend on the location of the site relative to the causative fault plane. The analysis also provided the main candidates for the worst case rupture scenarios of the pulse generation for the city of L'Aquila.

Keywords: ground motion pulses, dip-slip faulting, 2009 L'Aquila earthquake, focusing effect, worst case scenario.

1. INTRODUCTION

Observations from the past earthquakes demonstrated that ground motions recorded in the near-fault area can present significant differences from those observed at the larger distances from the seismic fault. Presence of strong coherent long-period ground motion pulses recorded at some of the stations corresponding to a specific geometry of the fault-station configuration was reported as being a distinctive characteristic of the near-fault ground motions, and was widely discussed in the previous studies (e.g., Aki 1968; Somerville *et al.*, 1997; Koketsu and Miyake, 2008). The rapid development of strong motion networks insured capturing of the long-period ground motion pulses in the vicinity of the seismic faults during the large damaging events like 1999 Kocaeli (M_w 7.6) earthquake, and the 1999 Chi-Chi (M_w 7.6) earthquake, as well as during smaller events such as 1994 Northridge (M_w 6.7), 1995 Kobe (M_w 6.9), and 2003 Bam (M_w 6.6) earthquakes. Most of them were associated with a significant amount of damage and loss of human lives. The engineering implication of these phenomena was revealed during the 1994 Northridge earthquake when the large velocity pulse like motion was found to be partly accountable for the considerable amount of damage to the good-quality buildings that were designed using the building code not taking into consideration any near source effects (e.g., Heaton *et al.*, 1995; Strasser and Boomer, 2009). An example illustrating the importance of including these near source effects into the building practice of critical facilities was given by the experience of the Kashiwazaki-Kariwa nuclear power plant during the 2007 Chuetsu-oki (M_w 6.6) earthquake in Japan (e.g., Miyake *et al.*, 2010).

The main cause of the near-fault long-period ground motion pulses observed at the near-source regions is considered to be the rupture directivity effect. This phenomenon can be observed in the case of both

strike-slip and dip-slip faulting. The rupture directivity effect appears as the result of the rupture front that propagates over a finite fault at a high speed, slightly less than the shear wave (S-wave) velocity of the media. If a site is located in the forward direction of the rupture most of the seismic energy of the wave front will arrive in a single pulse of motion (see Fig.1 for illustration). The conditions contributing to the forward directivity effects and the characteristics of the rupture directivity pulses were identified and summarized by Somerville *et al.* (1997) on the example of the near-fault record from the 1992 Landers earthquake (Fig. 2a). The theoretical aspects of the physical mechanism of their generation were addressed in a number of studies (e.g., Boore and Joyner, 1978, 1989; Heaton, 1990; Joyner, 1991; Miyatake, 1998). It was also pointed out that the forward directivity effect generates pulses with the dominant periods of 0.6 s or greater, that are strongly affecting the spectral content of the ground motions (e.g., Somerville *et al.*, 1997; Somerville, 2003; Koketsu and Miyake, 2008); thus, being able to place significant demands on structures in the near-fault regions. The study of Somerville (2003) indicated as well that the period of the pulse scales with the magnitude of the event. The later implying that even smaller earthquakes can place significant demands on structures in the near-fault regions.
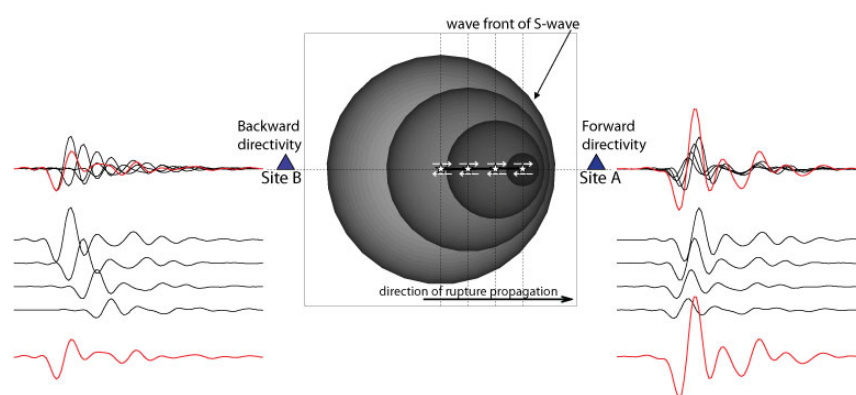
Figure 1. Illustration of the generation mechanism for the rupture directivity effects: snapshot of the wave fronts. Site A, located in the forward direction of the rupture propagation. Site B, located in the direction backward to the rupture propagation. The propagating rupture is represented by finite fault composed of four point sources (white stars) placed at distance R from each other; rupture is assume to start from the left most point, and propagate towards the right (black arrow) at a velocity $V_r = 0.9V_s$. The theoretically calculated synthetic waveforms from each of the subfaults (black traces), and the resulted total velocity waveforms (red traces) are shown for both sites A and B (blue triangles).

To demonstrate the effect that the near-fault ground motion pulses may have on the spectral characteristics of the ground motions (implicitly their contribution to the seismic hazard) we estimated the velocity response spectra of the fault normal components recorded at the two near-fault stations from the source region of the causative fault of the 1992 Landers (M_w 7.3) earthquake. The relative locations of the stations and the fault are presented in the Figure 2a. For the comparison we show both the record of the Lucerne station located in the forward direction of the rupture propagation, and recorded the corresponding long period pulse (Figs. 2a, b), and the backward directivity station of Joshua Tree (Figs. 2a, c). These records are representative of the effect of rupture directivity from a strike-slip fault, illustrating both the forward and backward directivity near-fault ground motions (Somerville *et al.*, 1997). We decomposed the velocity record from the Lucerne station into pulse and residual components by applying the wavelet decomposition method of Baker *et al.* (2007). Then, the corresponding velocity response spectra were calculated (Fig. 2b) for all three resulted ground motions. From the comparison of the response spectra it can be observed that the contribution to the large ordinates of the spectra at longer period range, around the pulse period (> 4 s) is coming from the pulse, while the response spectra of the residual waveform is roughly comparable to that of the station situated in the backward direction of rupture propagation (Fig. 2c). A similar analysis providing the similar results was performed for the strike normal (SN) component of the velocity record from the AQK hanging wall station (Fig. 2d) recorded during the 2009 L'Aquila, Italy (M_w 6.3) normal faulting

event (Fig. 2e). We observe a significant increment of spectral ordinates in the period range of ~1.8 s for the case of the 2009 L'Aquila earthquake. This interval also corresponds to the period range of the pulse recorded at the AQK station (Fig. 2b). The above examples illustrate that the near-fault ground motion pulses can produce larger demand to the structures than ordinary records. These also underline that the design criteria established without taking into account such long period near-field pulses will inevitably result in underestimation of observed ground motions.
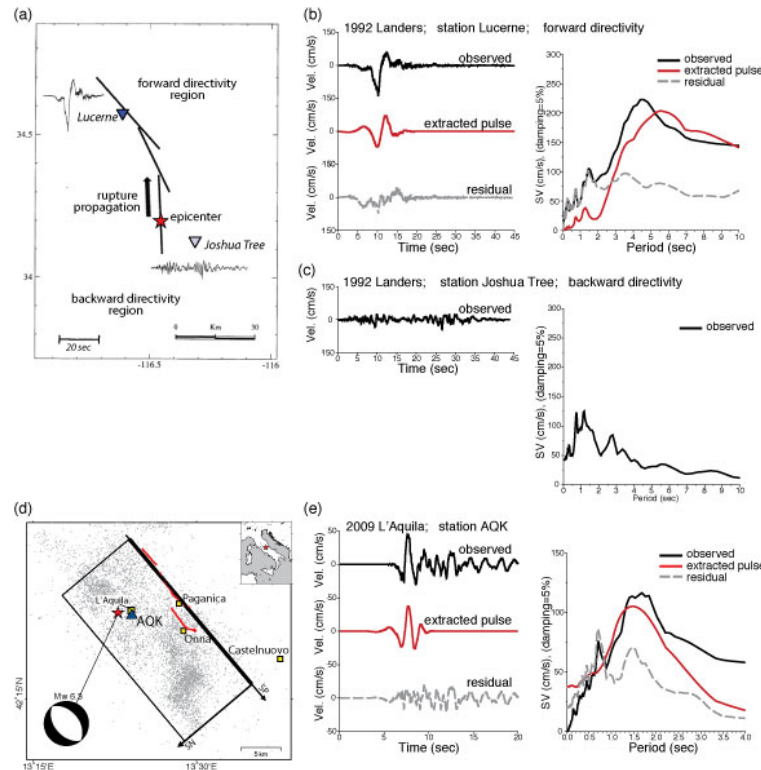
Figure 2. (a) Map view of the Landers region indicating faults ruptured during the 1992 Landers earthquake (modified from Somerville *et al.,* 1997). The red star shows the epicenter location, and the black arrow indicates the direction of rupture propagation. The fault normal ground velocities for the Lucerne with forward directivity and Joshua Tree with backward directivity stations are also shown. (b) Left: fault normal component of the velocity record (black) from Lucerne station recorded during the 1992 Landers earthquake. The extracted pulse (red trace) and the residual (gray trace) waveforms are shown below. Right: velocity response spectra of the corresponding time series. (c) Left: fault normal component of the velocity record the Joshua Tree station recorded during the 1992 Landers earthquake. Right: velocity response spectra of the corresponding time series. (d) Map view of the L'Aquila area indicating the location of the fault plane (black rectangle) ruptured during the 2009 L'Aquila earthquake. The red star indicates the location of the epicenter, the blue triangle shows the location of the near-fault hanging wall station AQK. (e) Left: Strike normal component of the velocity record (black) from the AQK station, recorded during the 2009 L'Aquila earthquake. The extracted pulse (red trace) and the residual (gray trace) waveforms are shown below. Right: Velocity response spectra of the corresponding time series.

The rupture directivity effect as described by Somerville *et al.* (1997) provide a good explanation of the fault normal components observed during the past strike-slip faulting events (e.g. 1992 Landers). In the case of the dip-slip faulting however, both the near-fault ground motion pulses and the hanging wall effect (Abrahamson and Somerville 1996) will be observed jointly for some of the stations. The inspection of the 3-D *S*-wave radiation patterns for dip-slip faulting (Fig. 3), as well as the near-fault strong ground motion records from the stations on the hanging wall sites above the causative fault of the 2007 Chuetsu-oki (reverse faulting; Miyake *et al.*, 2010) and 2009 L'Aquila (normal faulting) events, point towards a more complex mechanism for the pulse generation in the case of dip-slip faulting earthquakes.

In this study we inspected the main aspects of the rupture configuration that contribute to the generation of the near-fault ground motion pulses for a dip-slip faulting event, by performing the forward simulations for the different rupture scenarios for the case of the 2009 L'Aquila, Italy (M_w 6.3) damaging earthquake. We assumed rupture scenarios based on the broadband source model of the 2009 L'Aquila earthquake determined by Poiata *et al.* (2012), and performed the forward simulations of the waveforms for the near-fault strong motion stations in both broadband and low-frequency ranges.

2. NEAR-FAULT GROUND MOTION PULSES AND DIFFERENT FAULTING STYLES

An earthquake represents a shear dislocation propagating along the fault. The 3-D low-frequency radiation pattern of the *S*-wave generated by a point shear dislocation along the horizontal axes is shown in the Figure 3a (see e.g., Aki and Richards, 1980 for the full mathematical expression). It has been pointed out by a number of studies based on the high quality waveform records from the stations at both the near-field and intermediate distances from the seismic sources (e.g., Liu and Helmberger, 1985; Takenaka *et al.*, 2003; Takemura *et al.*, 2009) that in the higher frequency range of 1-3Hz the four lobbed radiation pattern of the S-wave is distorted. The distortion results in an isotopic distribution of *S*-wave amplitudes in all directions for the frequencies over 3 Hz (Liu and Helmberger, 1985). This phenomenon was attributed to the scattering of seismic waves by the heterogeneous structure around the source region ("heterogeneities in the source-process"; Liu and Helmberger, 1985) and along the propagation path of the seismic waves (Takemura *et al.*, 2009). Based on the results on these studies, and assuming some degree of simplification we represent the high-frequency radiation of *S*-wave generated by a point shear dislocation as a sphere (Fig. 3b). The limit between the low- and high-frequency ranges here is assumed at the frequencies of 1-3 Hz according to the results of the study by Liu and Helmberger (1985).

At the distances close to the earthquake fault, were the point source approximation is not valid, one has to take into consideration the fact that an earthquake is in fact a shear dislocation that propagates along a finite fault. Mathematically it is equivalent to a distribution (e.g., line distribution) of the point sources over the fault, and the propagation of the dislocation can be introduced by considering the appropriate time delays (e.g., Kasahara, 1981). The assumption will result in azimuth dependence of the rupture times observed at different locations of the observation point. This azimuth dependence due to fault propagation is called directivity (e.g., Aki and Richards, 1980; Lay and Wallace, 1998). The effect of the rupture directivity on the *S*-wave point source radiation pattern symmetry can be described by a factor called directivity function (e.g., Aki and Richards, 1980). The effects of the directivity on *S*-wave radiation pattern for low- and high-frequency range of a dip-slip fault are shown in the Figure 3d,e. The resulted elongation of the radiation pattern in the direction of rupture propagation will correspond to the forward directivity effect discussed in the Introduction section.

The occurrence of the forward rupture directivity effect at a given site is in general conditioned by a number of factors. These factors, as identified and summarized by Somerville *et al.* (1997) are following: rupture front must propagate towards the site, direction of slip on the fault must be aligned with the direction of rupture, rupture must propagate at a speed close to the velocity of *S*-wave. These conditions are most easily fulfilled in the case of the strike-slip faulting for which (in the most of the cases) rupture propagates horizontally along the strike, and the slip on the fault is oriented along the direction of the strike. It is also in good agreement with the fault normal components recorded during the past strike-slip faulting events (e.g., 1992 Landers earthquake; Fig. 2a). Following Somerville *et al.* (1997) it is possible to show that conditions for the forward directivity effect are also satisfied in case of dip-slip faulting, both reverse and normal faults (Fig. 3c). The alignment of the direction of rupture and the direction of slip along the dip of the fault (Figs. 3d,e) will generate the rupture directivity effect at the stations located close to the surface trace of the fault (Somerville *et al.*, 1997; Somerville, 2003). Figures 3d,e illustrate the above by showing the low- and high-frequency radiation patterns for an up-dip rupture propagation for the case of the normal faulting event. The rupture

directivity pulses in the case of dip-slip faulting will be observed in the direction normal to the dip of the fault, and will have its components in the vertical and horizontal directions normal to the strike.
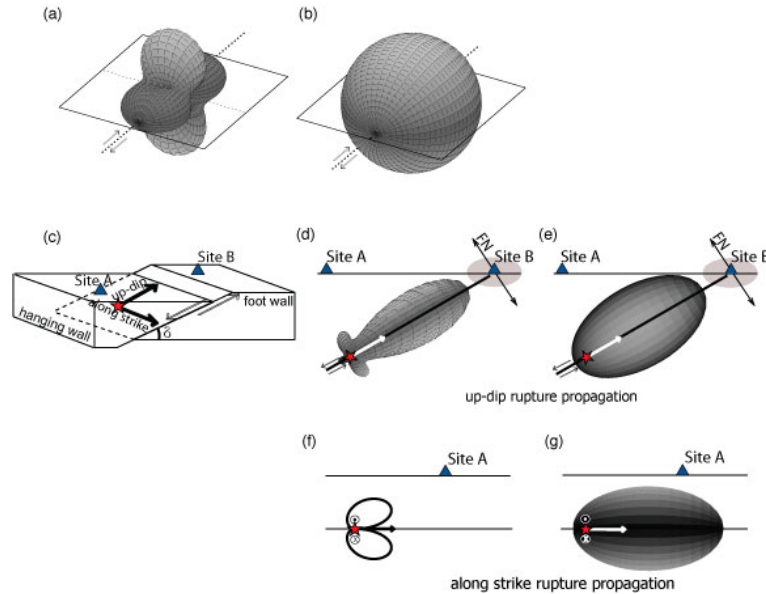
Figure 3. (a) 3-D low-frequency, and (b) high-frequency *S*-wave radiation patterns from a point source shear dislocation. The rectangles indicate the planes of faulting and the arrows show the directions of slip. (c) schematic illustration of a normal fault. The red star corresponds to the rupture starting point, the up-dip and along strike directions are shown by the full black arrows, and the directions of slip by the open arrows. The blue triangles indicate the location of the observation sites. Site A is located on the hanging wall side and above the rupture plane, and Site B is located on the foot wall side of the fault. (d) Vertical section of the low-frequency radiation pattern of the up-dip rupture propagation for the normal fault (c). The shaded area indicate the region of maximum forward directivity effect, and the black arrow show the orientation of the directivity pulses observed at the Site B. (e) Same as (d), but for the high-frequency range. (f) Vertical section of the low-frequency radiation pattern of the along strike rupture propagation for the normal fault (c). The direction of slip is shown in circles next to the rupture starting point (red star). (g) Same as (f), but for the high-frequency.

However, in the case of the dip-slip fault the plane of faulting normally forms an angle (δ – dip angle) with the horizontal plane (Fig. 3c). This geometrical configuration generates an area on the free surface that is located on the hanging wall side of the fault and above the ruptured plane. Considering the 3-D aspect of the *S*-wave radiation pattern (Fig. 3a, b) one must expect that a rupture propagating along the strike of a dip-slip fault could have some effect on the waveforms recorded by a station located on the hanging wall and above the rupture plane (Figs. 3f, g show the low- and high-frequency radiation patterns for along strike rupture propagation in the case of the normal faulting event). This implies that mechanism of pulse generation of a dip-slip faulting event could be more complex that the directivity effect described above following the Somerville *et al.* (1997). One of the supports for this idea can be considered the presence of the pulse-like velocity ground-motions at the records from near-fault stations located on the hanging wall side above the rupture plane of the recent 2009 L'Aquila (M_w 6.3) normal faulting event. The stations were not located near the surface trace of the fault were the forward directivity effect is expected to be maximum for a dip-slip fault. This situation is similar to the case of the record from the Kashiwazaki-Kariwa nuclear power plant during the 2007 Chuetsu-oki (M_w 6.6) reverse faulting earthquake (also pointed out by Kagawa, 2009).

3. CONDITIONS CONTRIBUTING TO THE GENERATION OF NEAR-FAULT PULSES: FORWARD SIMULATIONS FOR THE CASE OF 2009 L'AQUILA, ITALY, EARTHQUAKE

The 2009 L'Aquila, Italy (M_w 6.3) earthquake, provided an unprecedented for a normal faulting event amount of strong motion records in the near-fault area. We make use of this dataset as well as the results of the broadband source model (Fig. 4a) of Poiata *et al*. (2012) in order to get a better understanding of the conditions that contributed to the generation of the near-fault ground motion pulses recorded at the stations located on the hanging wall of the ruptured fault. The analysis is carried by performing the forward simulations for the different rupture scenarios. The main objectives that we followed through the analysis were: 1) compare the contribution of the along strike and up-dip propagation to the pulse generation; 2) determine the main aspects of the rupture configuration (direction of rupture propagation and the fault-station geometry) that contribute positively to the pulse generation; 3) identify the worst case rupture scenario for the city of L'Aquila.

We based our rupture scenarios on the strong motion generation area (SMGA) estimated using the Empirical Green's function (EGF) method by Poiata *et al*. (2012; Fig. 4), and performed the forward simulations of the waveforms for the near-fault strong motion stations in both broadband and low-frequency range. This option was selected in order to account for the difference in the radiation pattern in the low- and high-frequency range discussed in Section 2. The calculations are performed for both the stations located on the hanging wall side of the causative fault above the ruptured fault (AQ* stations, Fig. 4a), and the hanging wall stations located further distances away, as well as the foot wall station GSA. This selection of stations would provide more detailed information on the spatial variability of the near-fault ground motion pulses (fault-station geometry). Here, we present the results of analysis on the example of the AQU hanging wall station, and GSA foot wall station.
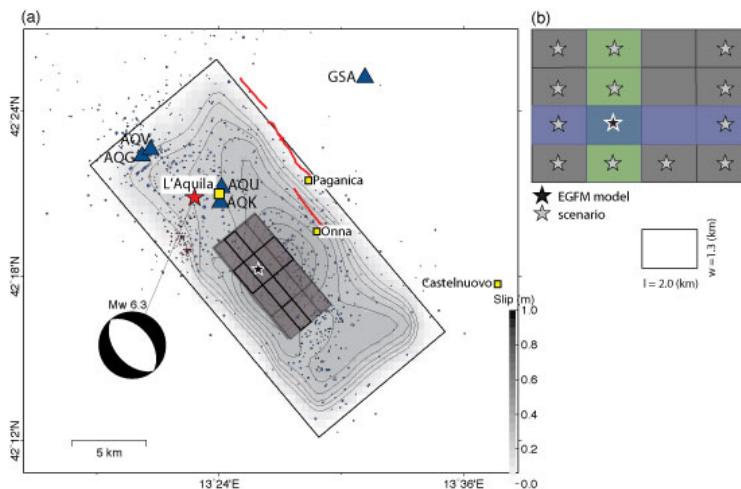
Figure 4. (a) Map view of the L'Aquila area presenting the relative location of the surface projection of the rupture plane for the 2009 L'Aquila earthquake (after Poiata *et al*., 2012) and the near-fault hanging wall (AQG, AQV, AQU and AQK) and foot wall (GSA) stations. The red star indicates the location of the epicenter reported by INGV. The gray rectangle corresponds to the SMGA estimated from the EGF analysis of Poiata *et al*, (2012). The areas delimited by the green and blue rectangles correspond to the two rupture scenarios of the up-dip and the along-strike rupture propagations used in the forward simulation analysis of the near-fault pulses. (b) Plane view of the fault settings for the rupture scenarios used for the forward simulations: rupture scenarios for the different rupture starting points.

The broadband calculations (0.2-10 Hz) were performed using the EGF method of Irikura *et al.* (1986); and the low-frequency (0.05-0.5 Hz) synthetic waveforms were deterministically calculated using the extended reflectivity method of Kohketsu (1985). The parameters of the EGF event (the M_w 4.6 aftershock from 7 April 2009, 21:34:29) used for the broadband forward modeling, the 1-D velocity models of the low-frequency calculations, as well as the parameters for the SMGA are those of Poiata *et al*. (2012). We do not describe the above parameters in detail here due to the size limitation of the paper. The source model (number and size of subfaults) for the low-frequency simulation was assumed based on the SMGA. The value of the rise time for the ramp source time function and the seismic moment for each subfault were estimated through the forward modeling of

the M_w 4.6 aftershock for the near-fault hanging wall stations shown in Figure 4a. The resulted values correspond to the seismic moment $M_0 = 2.3 \times 10^{15}$ Nm, and the rise time $\tau = 1.0$ s (this values correspond to a single subfault not the entire rupture area). The velocity of the rupture propagation is set to 2.9 km/sec (~0.85V_S), same as for the broadband modeling. The settings for the rupture scenarios are summarized in Figure 4b. We tested the contribution of the along strike versus up-dip rupture propagation for the SMGA of the EGF model, the effect of the different assumptions for the locations of the rupture starting point (Fig. 4b), and the location of the rupture area relative to the city of L'Aquila (Fig. 5a). For the later one the AQU station was selected as representative, since no records were available from the historical center of the city of L'Aquila (most damaged area of the city).

The results of the forward simulations identified that: 1) both the up-dip and the along-strike rupture propagations contribute to the generation of the near-fault ground motion pulses with the up-dip rupture propagation contribution being more significant, and 2) the conditions for the pulse generation that could be identified for all stations (hanging wall or foot wall) is that the rupture should propagate into the direction towards the site. The forward simulations for the different rupture scenarios showed that for the near-fault stations (both hanging wall and foot wall) not located above the rupture plane (e.g., GSA station Fig. 5d) both the along strike and up-dip rupture propagations contribute to the pulse generation. The main conditions for the pulse generation for this stations that could be identified is that the direction of rupture propagation should be towards the site. Figure 5d illustrates this conclusion on the example of the GSA station located on the foot wall side of the causative fault. The finding is supported by both the broadband and low-frequency synthetics. We could not identify predominant direction of pulse generation for these stations. We will discuss next in more detail the results of the forward simulations for the rupture scenarios assuming the different locations for the rupture starting point (Figs. 5b, c) and the positions of the rupture area for the case of the near-fault stations positioned on the hanging wall above the ruptured fault (AQ* stations from the Aterno Valley).

3.1. Near-fault hanging wall stations located above the ruptured fault

Figure 5 show the examples of rupture scenarios assuming the rupture of the entire SMGA and the different locations of the rupture stating point. These scenarios will result in different directions of rupture propagation relative to the AQ* stations. In case 1 rupture will propagate towards the stations, and the fraction of the ruptured area of the fault between the hypocenter and the stations will be maximum; while in Case 2 rupture will propagate away from the stations, and the fraction of the ruptured area of the fault between the hypocenter and the stations will be minimum. The results of the forward simulations for the broadband and the low-frequency range (Fig. 5c) show that the near-fault ground motion pulses are generated for the scenarios implying the propagation of rupture towards the stations. We could also confirm that the amplitude of the pulses for both the broadband and the low-frequency components of the station AQU are maximum when the scenario corresponding to the rupture starting point located in the lower right end of the fault is assumed (Case 1, Fig. 5c). This scenario includes the along-strike (predominant) and up-dip propagation of rupture in the direction of the station. We will refer to this rupture scenario as "rupture propagation toward the site" in order to distinguish it from the rupture directivity effect.

The rupture scenario assuming the different location of the rupture area (SMGA) relative to the AQ* stations, were mainly targeted in the search for the worst case scenario of the pulse generation for the city of L'Aquila. Here we focused on the synthetic waveforms at the AQU station. We could identify two cases for the locations of the rupture area and the rupture starting point relative to the AQU station that result in most significant contribution to the pulse generation for both the broadband and low-frequency synthetic waveforms. These rupture scenarios are summarized in Figure 6, showing their relative location to the AQU stations. It can be observed that the first scenario (Case 1) correspond to the rupture propagation towards the station discussed above (Fig. 5a-c, Case 1), while the second scenario (Figs. 5a-c and 6, Case 3) represent the case when the station (AQU) is located above the rupture plane and the distance to the rupture stating point is shortest (Fig. 5b, right). This case

corresponds to the "focusing effect" discussed as well by Kagawa (2009). The effect is caused by the simultaneous arrival of the rupture front from the different points of the fault, located at the same distance (on the same isochrones) from the rupture starting point (see Figure 7b). The synthetic broadband and low-frequency waveforms for the Cases 1 and 3 are presented in the Figs. 5c and 6a. It can be observed (Fig. 6a) that both of the rupture propagation towards the site (case 1), and the focusing effect (Case 3) generate the ground motion pulses that are significantly exceeding the observations as well as the synthetics for the SMGA of the EGF model (Fig. 6a). The comparison of the velocity response spectra for the observed and synthetic waveforms (Figs. 6c, d) indicate that in the period range of 2.0-3.5s for both cases the spectral ordinates of the observed ground motions are significantly below the level provided by the two scenarios. However, for Case 3 (focusing effect) significantly higher than observed spectral value is indicated for the period around 1.0-1.3 s (Fig 6c), corresponding to the resonance period of the typical residential buildings in the area. The comparison presented above indicates that the actual 2009 L'Aquila earthquake did not constitute the worst case for the city, regardless of its proximity to the epicenter of the mainshock.
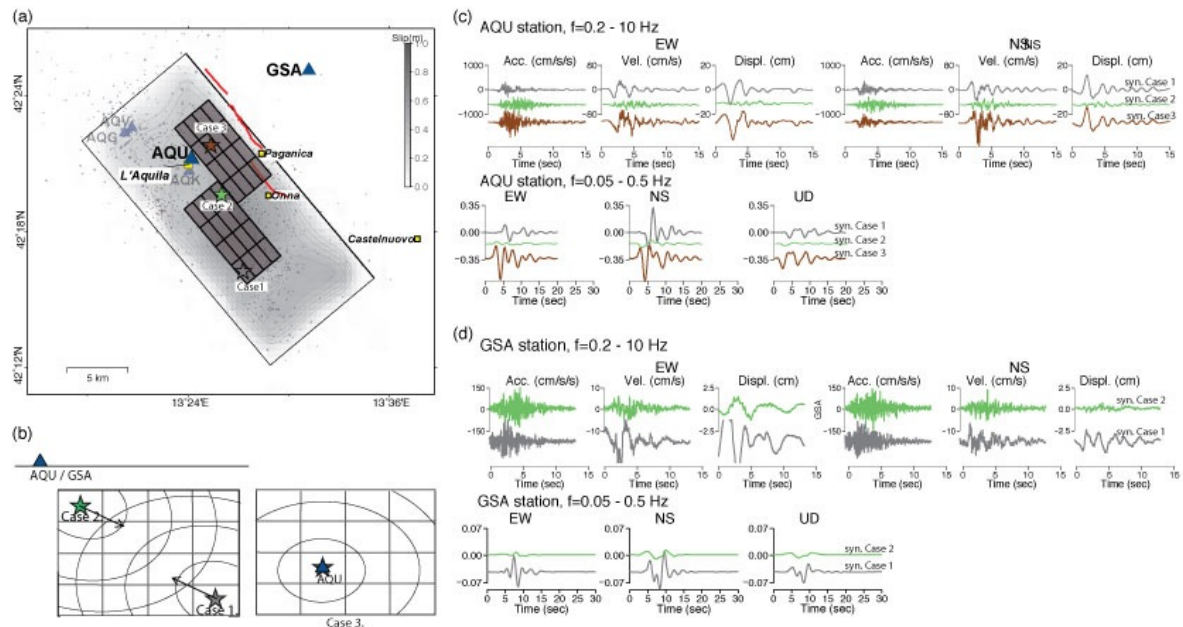
Figure 5. (a) Map view showing the relative location of the AQU and GSA stations (blue triangles) and the rupture scenario corresponding to the predominant along-strike rupture propagation (Cases 1 and 2; rupture starting points are shown by the gray and green stars respectively), and the focusing effect (Case 3; rupture starting point is shown by the brown star). (b) Vertical view of the rupture scenarios. The stars correspond to the location of the rupture starting points. The blue triangle shows the station location. (c) and (d) synthetic broadband and low-frequency waveforms for the rupture scenarios of Case 1 (gray traces), Case 2 (green traces), and Case 3 (brown traces) of the stations AQU and GSA, respectively.

4. CONCLUSIONS

Ground motion pulses observed at the stations corresponding to a specific geometry of the fault-station configuration represent one of the distinctive characteristics of the near-fault records. These pulses can strongly affect the duration and spectral content of the ground motions, producing larger demand to the structures than ordinary records. The forward rupture directivity effect is generally considered to be the main cause of near-fault ground motion pulses observed in the near source regions of both strike-slip and dip-slip faulting. The conditions for the rupture directivity effects summarized by Somerville *et al.* (1997) provide a good explanation of the fault normal components observed during the past strike-slip faulting events (e.g., 1992 Landers). In the case of the dip-slip faulting however, both the near-fault ground motion pulses and the hanging wall effect (Abrahamson and Somerville 1996) will be observed jointly for some of the stations. The inspection of the 3-D *S*-wave radiation

patterns for dip-slip faulting, as well as the near-fault strong ground motion records from the stations on the hanging wall sites above the causative fault of the 2007 Chuetsu-oki (reverse faulting) and 2009 L'Aquila (normal faulting) events, point towards a more complex mechanism for the pulse generation.
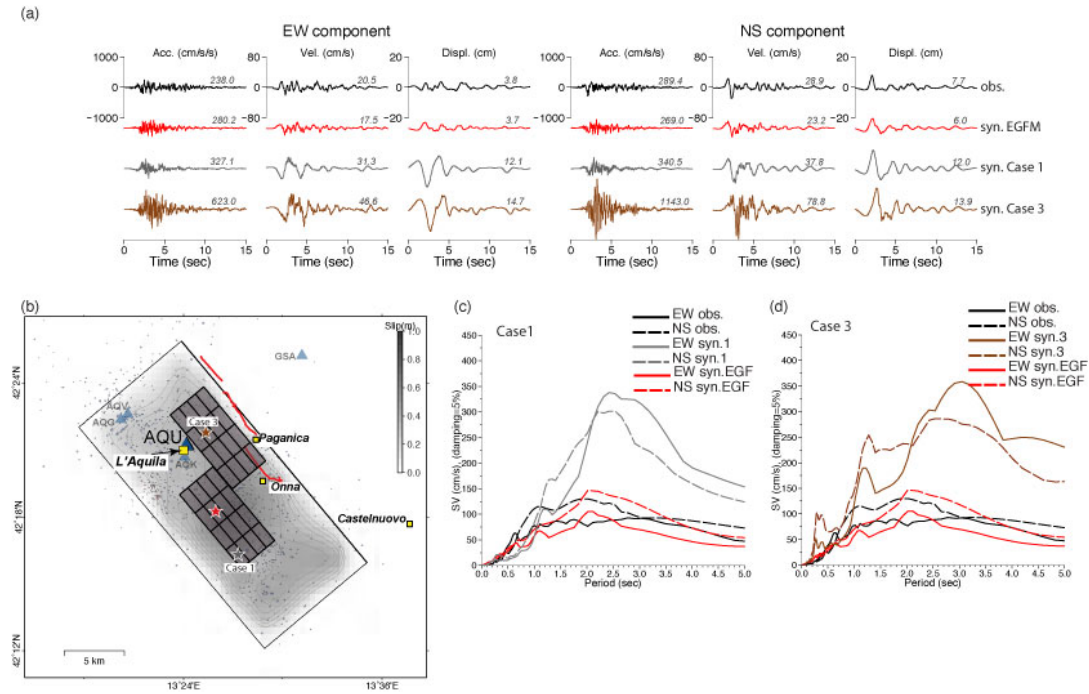
Figure 6. (a) Comparison of the observed (black traces) acceleration, velocity, and displacement waveforms for the horizontal components of the broadband record of 2009 L'Aquila mainshock from the AQU station, and the synthetics calculated for the SMGA by the EGF simulation of Poiata *et al.* (2012; red traces), the rupture scenario of the rupture propagation towards the AQU station (Case 1; gray traces), and the rupture scenario corresponding to the case of the focusing effect (Case 3; brown traces). The numbers above the waveforms correspond to the maximum amplitudes. (b) Map view of the near-fault area of the 2009 L'Aquila earthquake showing the relative location of the AQU station (blue triangle), the city of L'Aquila, and the rupture areas for the assumed scenario and EGF model (gray rectangles). The stars correspond to the location of the rupture starting points. (c) and (d) 5% damped velocity response spectra comparing the observed horizontal components of the AQU record (in black), and the synthetics calculated for the two cases of the rupture scenarios and the EGF model (red traces).

In this study, we inspected the main aspects of the rupture configuration that contribute to the generation of the near-fault ground motion pulses for a dip-slip faulting event, by performing the forward simulations for the different rupture scenarios for the case of the 2009 L'Aquila, Italy (M_w 6.3) damaging earthquake. We assumed rupture scenarios based on the broadband source model of the 2009 L'Aquila earthquake determined by Poiata *et al.* (2012), and performed the forward simulations of the waveforms for the near-fault strong motion stations in both broadband and low-frequency range. The results of our analysis indicate that the generation mechanism of the near-fault ground motion pulses in the case of dip-slip faulting depends on both the rupture configuration and the location of the site relative to the fault plane. We could confirm that the rupture directivity effect is predominant for the stations located on the foot wall of the causative fault. For all of the hanging wall stations the radial rupture propagation towards the site (Fig. 7a) is representing the main condition of ground motion pulse generation. However, for the stations located on the hanging wall above the rupture plane where the hanging wall effect is observed (Abrahamson and Somerville, 1996), the focusing effect (Kagawa, 2009) could be identified as being another mechanism for the pulse generation. The analysis also pointed out that the along-strike propagation towards the site and the focusing effect (Fig. 7) are the main candidates for the worst case rupture scenarios of the pulse generation for the city of L'Aquila (Fig. 6).
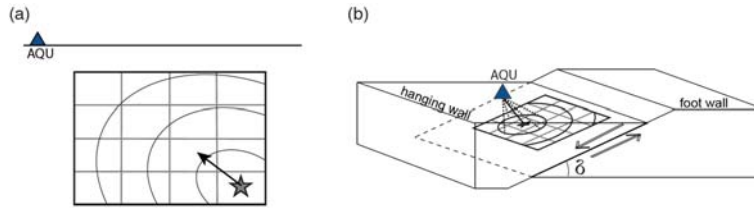
Figure 7. Schematic illustration of (a) radial rupture propagation towards the site and (b) focusing effect.

REFERENCES

Abrahamson, N. A., and P. G. Somerville (1996). Effects of the hanging wall and footwall on ground motions recorded during the Northridge earthquake, *Bull. Seismol. Soc. Am.* **86**, S93-S99.

Aki, K. (1968). Seismic displacement near a fault, *J. Geophys. Res.* **73**, 5359–5376.

Aki, K., and P. G. Richards (1980). *Quantitative Seismology*, W. H. Freeman, San Francisco, 932 pp.

Baker J.W. (2007). Quantitative classification of near-fault ground motions using wavelet analysis. *Bull. Seismol. Soc. Am.* **97**, 1486-1501.

Baker J.W. and S. Shahi. Quantitative Classification of Near-Fault Ground Motions Using Wavelet Analysis (supporting software). http://www.stanford.edu/~bakerjw/pulse-classification.html.

Boore, D. M., and W. B. Joyner (1978). The influence of rupture incoherence on seismic directivity, *Bull. Seismol. Soc. Am.* **68**, 283-330.

Boore, D. M., and W. B. Joyner (1989). The effect of directivity on the stress parameter determined from ground motion observations, *Bull. Seismol. Soc. Am.* **79**, 1984-1988.

Heaton, T. H. (1990). Evidence for and implications of self-healing pulses of slip in earthquake rupture, *Phys. Earth Planet. Inter.* **64**, 1-20.

Heaton, T. H., D. F. Hall, D. J. Wald, and M. W. Halling (1995). Response of high-rise and base-isolated buildings to a hypothetical *M* 7.0 blind thrust earthquake, *Science* **267**, 206–211.

Irikura, K. (1986). Prediction of strong acceleration motions using empirical Green's function, *Proc. 7th Japan Earthq. Eng. Symp.*, 151-156.

Joyner, W. B. (1991). Directivity for nonuniform ruptures, *Bull. Seismol. Soc. Am.* **81**, 1391-1495.

Kagawa T. (2009). Conditions of fault rupture and site location that generate damaging pulse waves, *Proceedings of the 6th International Conference on Urban Earthquake Engineering*, 53-58.

Kasahara, K. (1981). *Earthquake Mechanics,* Cambridge University Press, 248 pp.

Kohketsu, K. (1985). The extended reflectivity method for synthetic near-field seismograms, *J. Phys. Earth* **33**, 121-131.

Koketsu, K., and H. Miyake (2008). A seismological overview of long-period ground motion, *J. Seismol.* **12**, 133-143.

Lay, T., and T. C. Wallace (1995). *Modern Global Seismology*, Academic Press, San Diego, 521 pp.

Liu, H., and D.V. Helmberger (1985). The 23:19 aftershock of the 15 October 1979 Imperial valley earthquake: more evidence for an asperity, *Bull. Seismol. Soc. Am.*, **75**, 689–708.

Miyake, H., K. Koketsu, K. Hikima, M. Shinohara, and T. Kanazawa (2010). Source fault of the 2007 Chuetsu-oki, Japan, earthquake, *Bull. Seismol. Soc. Am.* **100**, 384-391.

Miyatake, T. (1998). Generation Mechanism of Strong Ground Motion Pulse Near the Earthquake Fault, *Zisin2* **51**, 161-170 (in Japanese with English abstract).

Poiata, N., K. Koketsu, A. Vuan, and H. Miyake (2012). Low-frequency and broadband source models for the 2009 L'Aquila, Italy, earthquake, *Geophys. J. Int.*, in revision.

Somerville P. G. (2003). Magnitude scaling of the near fault rupture directivity pulse, *Phys Earth Planet Inter.* **137**, 201–212.

Somerville, P. G., N. F. Smith, R. W. Graves, and N. A. Abrahamson (1997). Modification of empirical strong ground motion attenuation relations to include the amplitude and duration effects of rupture directivity, *Seismol. Res. Lett.* **68**, 199–222.

Strasser, F. O., and J. J. Bommer (2009). Review: Strong ground motions—Have we seen the worst?, *Bull. Seismol. Soc. Am.* **99**, 2613-2637.

Takemura S, T. Furumura, and T. Saito (2009). Distortion of the apparent S-wave radiation pattern in the high-frequency wavefield: Tottori-Ken Seibu, Japan, earthquake of 2000. *Geophys. J. Int.,* **178**(2), 950-961.

Takenaka, H., Y. Mamada, and H. Futamure (2003). Near-source effect on radiation pattern of high-frequency S waves: strong SH–SV mixing observed from aftershocks of the 1997 Northwestern Kagoshima, Japan, earthquakes, *Phys. Earth planet. Int.*, **137**, 31–43.